Electronic Supplementary Information

2D Molecular Crystal Templated Organic p-n Heterojunctions for High-Performance Ambipolar Organic Field-Effect Transistors

Siyu Guo,‡[a] Jiarong Yao,‡[a] Ying Wang,[a] Lijuan Zhang,[a] Fei Zhai,[b] Xiali Zhang,[c] Yiyu Feng,[b] Wei Feng,[b] Xiaotao Zhang,[a] Jiansheng Jie,[c] Fangxu Yang,[a] Rongjin Li*[a] and Wenping Hu[a]*

[a] Tianjin Key Laboratory of Molecular Optoelectronic Sciences, Department of Chemistry, School of Science, Tianjin University & Collaborative Innovation Center of Chemical Science and Engineering, Tianjin 300072, China.
[b] School of Materials Science and Engineering, Tianjin University, Tianjin 300072, China
[c] Institute of Functional Nano & Soft Materials (FUNSOM), Jiangsu Key Laboratory for Carbon-Based Functional Materials & Devices Soochow University, Suzhou 215123, China.

E-mail: yangfangxu@tju.edu.cn; lirj@tju.edu.cn

Contents

Table S1 Unipolar thin film OFETs of $F_{16}CuPc$.

Method	Fabrication condition	Mobility ($cm^2 V^{-1} s^{-1}$)	Ref.
Thermal evaporation	Substrate temperature = 125°C	0.03	1
Thermal evaporation	Substrate temperature = 120°C	0.011	2
Thermal evaporation	With silk fibroin as the gate dielectric	0.39	3
Thermal evaporation	With C_{60} as floating gate layer on a flexible substrate	0.0018	4
Thermal evaporation	*p*-6P film served as the inducing layer Substrate temperature = 110°C	0.27	5
Thermal evaporation	*p*-6P film served as the inducing layer Substrate temperature = 150°C	0.12-0.5	6

Table S2 Bilayer aOFETs adopting $F_{16}CuPc$ as the n-type semiconductor.

P type material	$\mu_{h, max}$ ($cm^2 V^{-1} s^{-1}$)	Device structure	Preparation method	$\mu_{e, max}$ ($cm^2 V^{-1} s^{-1}$)	Ref.
CuPc	1×10^{-6}	CuPc(10 nm)/Au/$F_{16}CuPc$(2 nm)/SiO_2	Thermal evaporation	1×10^{-6}	7
CuPc	1.44×10^{-3}	Au/CuPc(30 nm)/$F_{16}CuPc$(10 nm)/SiO_2	Thermal evaporation	9.97×10^{-4}	8
CuPc	7.8×10^{-4}	Au/$F_{16}CuPc$(25 nm)/CuPc(5 nm) /SiO_2	Thermal evaporation	4.6×10^{-4}	9
BP2T	4.0×10^{-2}	Au/$F_{16}CuPc$(20 nm)/BP2T(3 nm) /SiO_2	Thermal evaporation	3.6×10^{-2}	10
CuPc	N/A	$F_{16}CuPc$(10 nm)/ Au/CuPc(20 nm)/SiO_2	Thermal evaporation	1.12×10^{-2}	11
p-6P	N/A	Au/$F_{16}CuPc$ (20 nm)/*p*-6P (1 nm) /SiO_2	Thermal evaporation	1.1×10^{-1}	12
BP2T	1.2×10^{-1}	Au/$F_{16}CuPc$(20 nm)/BP2T(5 nm) /SiO_2	Thermal evaporation	2.5×10^{-2}	13
CuPc	2.96×10^{-3}	Au/$F_{16}CuPc$(5 nm)/CuPc(15 nm)/SiO_2	Thermal evaporation	9.49×10^{-3}	14
PhT2	3.4×10^{-2}	Au/$F_{16}CuPc$(20 nm)/PhT2(2 nm)/SiO_2	Thermal evaporation	3.0×10^{-2}	15
CuPc	2.91×10^{-2}	Au/CuPc(20 nm)/$F_{16}CuPc$(5 nm)/OTS-SiO_2	Thermal evaporation	1.04×10^{-2}	16
CuPc	7×10^{-2}	Au/$F_{16}CuPc$(87 nm)/CuPc(56 nm)/OTS-SiO_2	Physical vapor transport	5×10^{-2}	17
CuPc	1.30×10^{-3}	Au/CuPc(10 nm)/$F_{16}CuPc$(10 nm)/SiO_2	Thermal evaporation	1.30×10^{-2}	18
CuPc	3.1×10^{-3}	Au/MoO_3/CuPc(7 nm)/$F_{16}CuPc$(27 nm)/SiO_2	Thermal evaporation	2.5×10^{-3}	19
C_{10}-DNTT	8.97	Au/$F_{16}CuPc$(20 nm)/C_{10}-DNTT/SiO_2	$F_{16}CuPc$ by thermal evaporation, C_{10}-DNTT by dual solution shearing	6×10^{-2}	20
CuPc	2.6×10^{-2}	$F_{16}CuPc$(5 nm)/CuPc(11 nm)/Pt/SiO_2	Thermal evaporation	1.4×10^{-2}	21
C6-DPA	3.97	$F_{16}CuPc$(10 nm)/Au/C6-DPA(9 nm)/SiO_2	$F_{16}CuPc$ by thermal evaporation, C6-DPA by SCS	5.6×10^{-1}	This work

Table S3 The threshold voltages of the OFETs.

Device	V_{th} (V)
C6-DPA (p-type)	-13
Heterojunction (p-channel)	1
$F_{16}CuPc$ (n-type)	20
Heterojunction (n-channel)	5

The threshold voltages of the OFETs were deduced from Fig. S12b, Fig. 4b, Fig. S11b, and Fig. 4c, respectively.

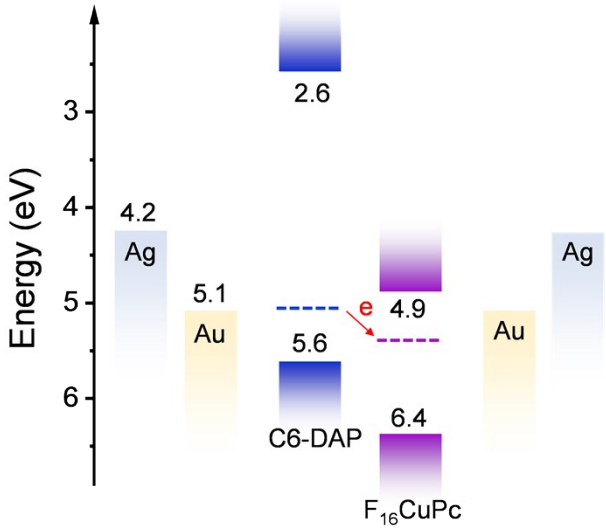

Fig. S1 A schematic energy level diagram of the $F_{16}CuPc$ and C6-DPA.[22-23]

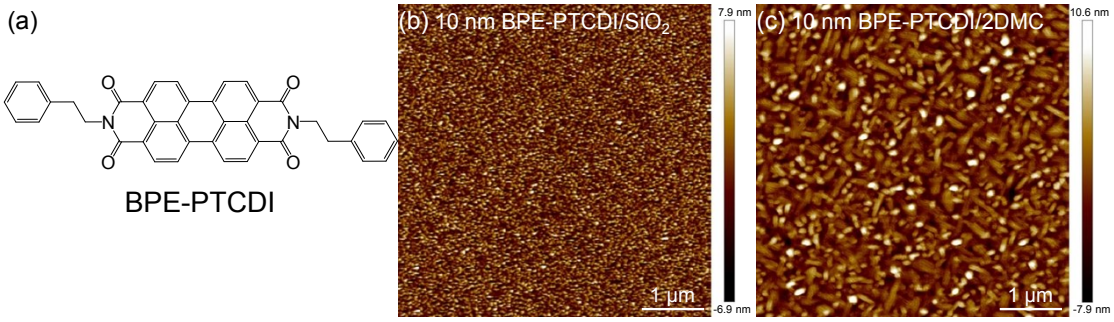

Fig. S2 (a) The chemical structure of BPE-PTCDI. AFM images of (b) 10 nm BPE-PTCDI deposited on SiO_2, (c) 10 nm of BPE-PTCDI deposited on 2DMC of C6-DPA, respectively.

BPE-PTCDI (10 nm) deposited on SiO_2/Si exhibited small and randomly-oriented spherical grains with high density of grain boundaries (Fig. S2b). The morphology changed prominently when BPE-PTCDI (10 nm) was deposited on 2DMC of C6-DPA (Fig. S2c).

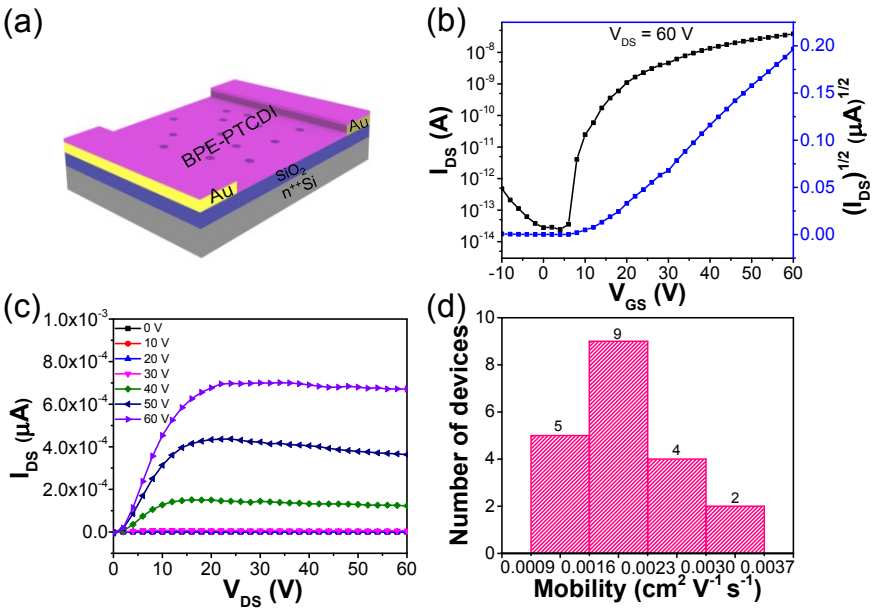

Fig. S3 (a) Schematic of an OFET of BPE-PTCDI. (b) Typical transfer and (c) output curves of BPE-PTCDI. The channel length was 110 μm and the channel width was 131 μm. (d) Histogram of the mobility of 20 BPE-PTCDI OFETs. The average electron mobility was 2.02 × 10^{-3} cm^2 V^{-1} s^{-1} among 20 devices, and the highest value was 3.46 × 10^{-3} cm^2 V^{-1} s^{-1}.

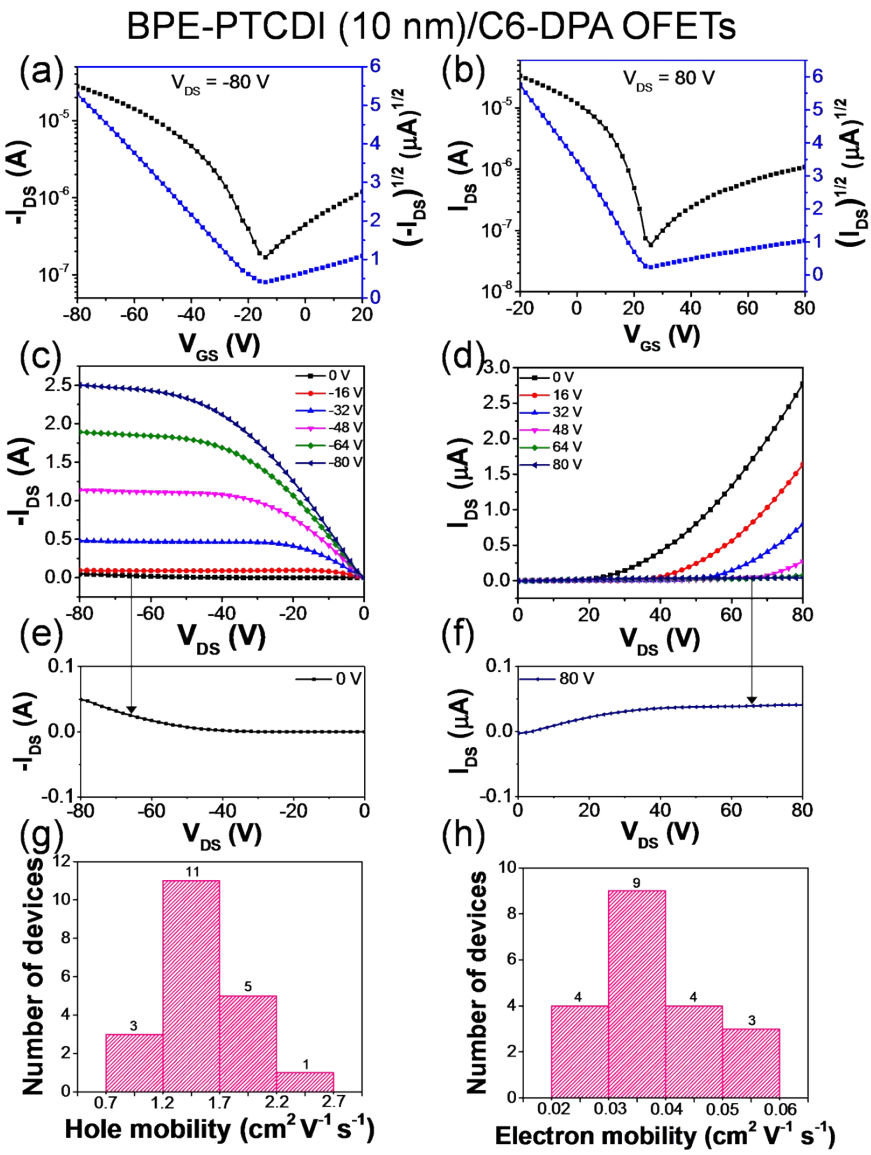

Fig. S4 (a) Typical transfer and (c) output characteristics of p-channel operation mode under negative drain bias. (b) Typical transfer and (d) output characteristics of n-channel operation mode under positive drain bias. The channel length was 117 μm and the channel width was 136 μm. (e and f) Magnified output characteristics of p-channel operation mode of (c) at V_{GS} = 0 V and n-channel operation mode of (d) at V_{GS} = 80 V, respectively. (g and h) Mobility distribution of BPE-PTCDI (10 nm)/C6-DPA aOFETs in p-channel operation mode and n-channel operation mode, respectively.

The maximum (average) mobility for p-channel and n-channel was 2.61 (1.60) cm^2 V^{-1} s^{-1} and 5.60 × 10^{-2} (3.85 × 10^{-2}) cm^2 V^{-1} s^{-1}, respectively. It was noted that the mobility of BPE-PTCDI increased over one order of magnitude compared with that of the unipolar devices (Fig. S3).

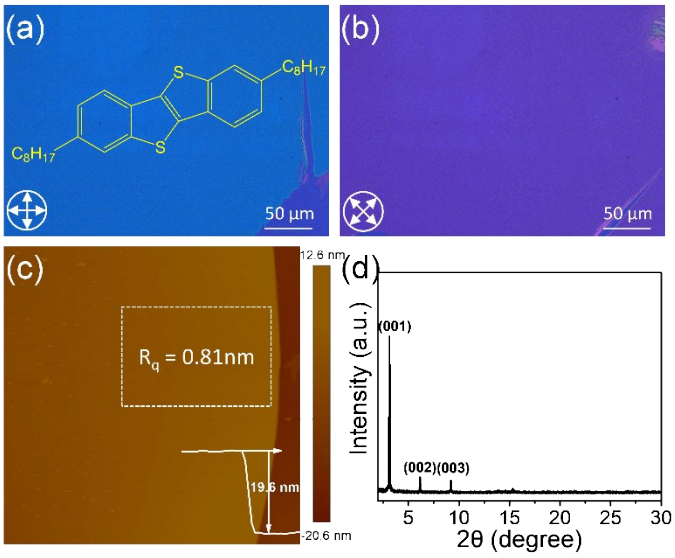

Fig. S5 (a and b) POM images, (c) AFM image and (d) XRD of a 2DMC of C8-BTBT.

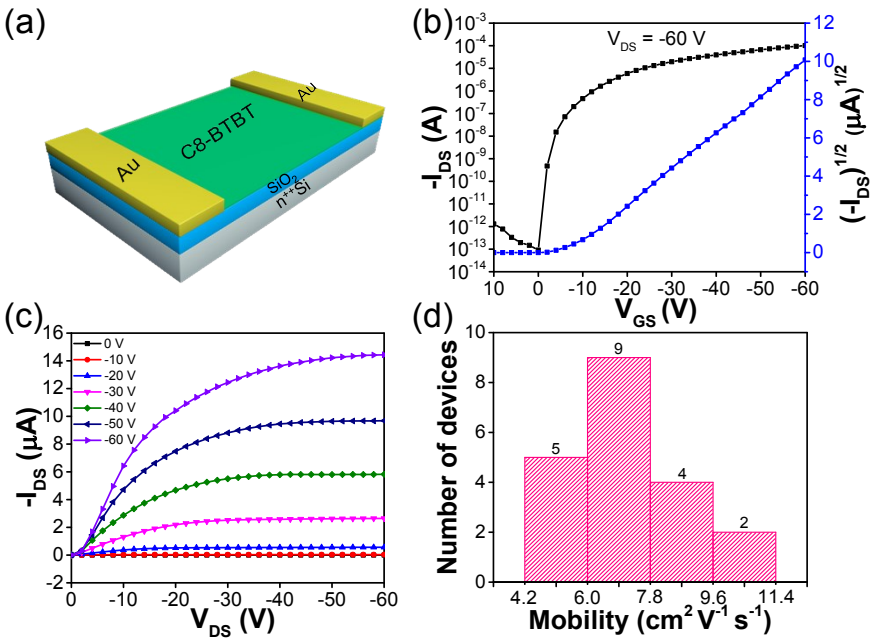

Fig. S6 (a) Schematic of an OFET of C8-BTBT. (b) Typical transfer and (c) output curves of C8-BTBT. The channel length was 161 μm and the channel width was 139 μm. (d) Histogram of the mobility of 20 C8-BTBT OFETs. The average electron mobility was 7.07 $cm^2 V^{-1} s^{-1}$ among 20 devices, and the highest value was 11.33 $cm^2 V^{-1} s^{-1}$.

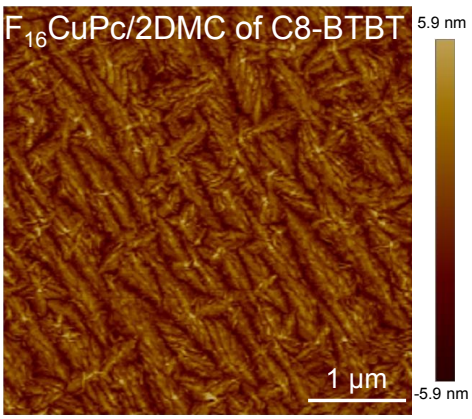

Fig. S7 AFM image of F_{16}CuPc (15 nm) deposited on 2DMC of C8-BTBT. F_{16}CuPc deposited on 2DMCs of C8-BTBT also exhibited micrometer-sized grains (grain size ≈ 0.3~1.6 μm).

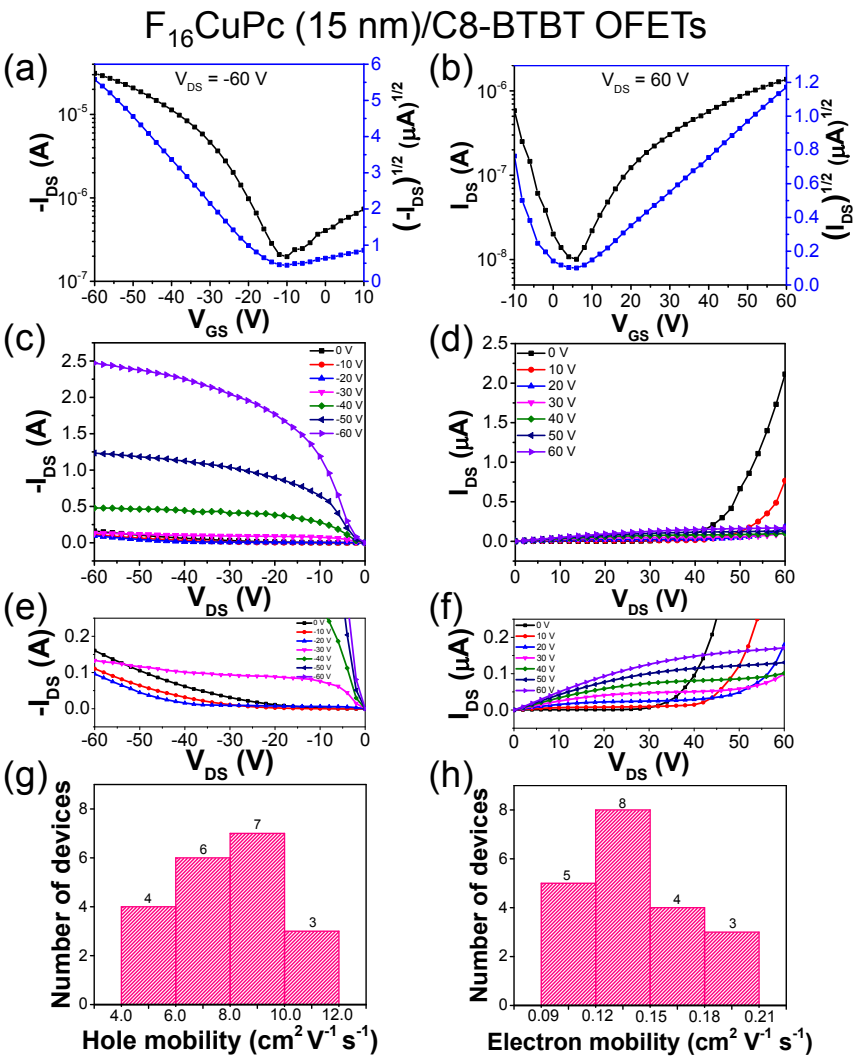

Fig. S8 (a) Typical transfer and (c) output characteristics of p-channel operation mode under

negative drain bias. (b) Typical transfer and (d) output characteristics of n-channel operation mode under positive drain bias. The channel length was 149 μm and the channel width was 102 μm. (e and f) Magnified output characteristics of p-channel operation mode and n-channel operation mode, respectively. (g and h) Mobility distribution of $F_{16}CuPc$ (15 nm)/C8-BTBT aOFETs in p-channel operation mode and n-channel operation mode, respectively.

The maximum (average) mobility for p-channel and n-channel was 11.77 (7.35) $cm^2 V^{-1} s^{-1}$ and 0.20 (0.13) $cm^2 V^{-1} s^{-1}$, respectively. It was noted that the mobility of $F_{16}CuPc$ increased about one order of magnitude compared with that of the unipolar devices (Fig. S11).

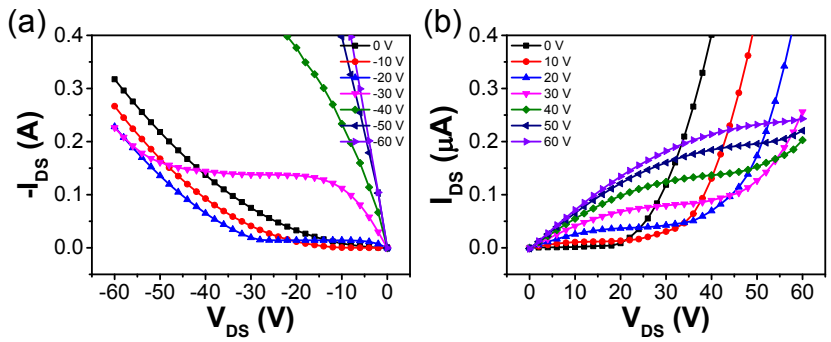

Fig. S9 (a and b) Magnified output characteristics of $F_{16}CuPc$ (10 nm)/C6-DPA aOFET of Fig. 4 (d and e), respectively.

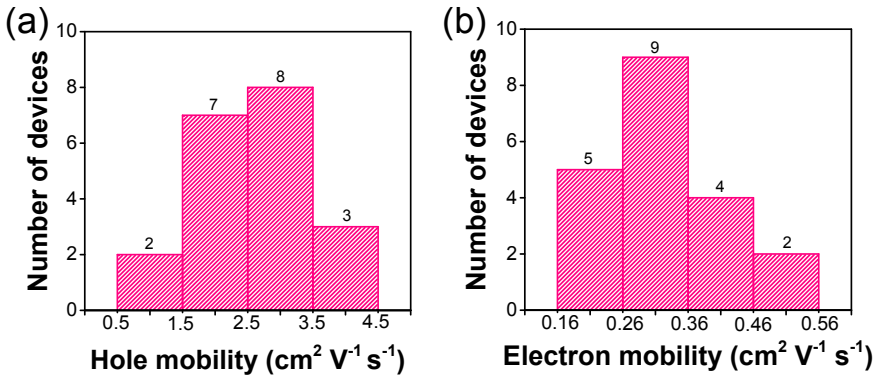

Fig. S10 (a and b) Mobility distribution of $F_{16}CuPc$ (10 nm)/C6-DPA aOFETs in p-channel operation mode and n-channel operation mode, respectively.

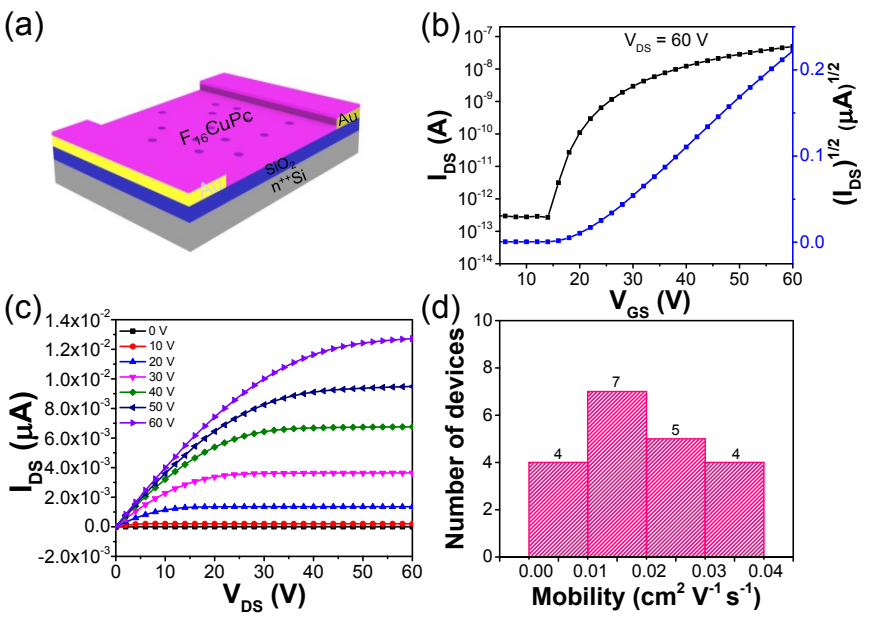

Fig. S11 (a) Schematic of an OFET of $F_{16}CuPc$. (b) Typical transfer and (c) output curves of $F_{16}CuPc$. The channel length was 116 μm and the channel width was 93 μm. (d) Histogram of the mobility of 20 $F_{16}CuPc$ OFETs. The average electron mobility was 1.95×10^{-2} cm^2 V^{-1} s^{-1} among 20 devices, and the highest value was 3.60×10^{-2} cm^2 V^{-1} s^{-1}.

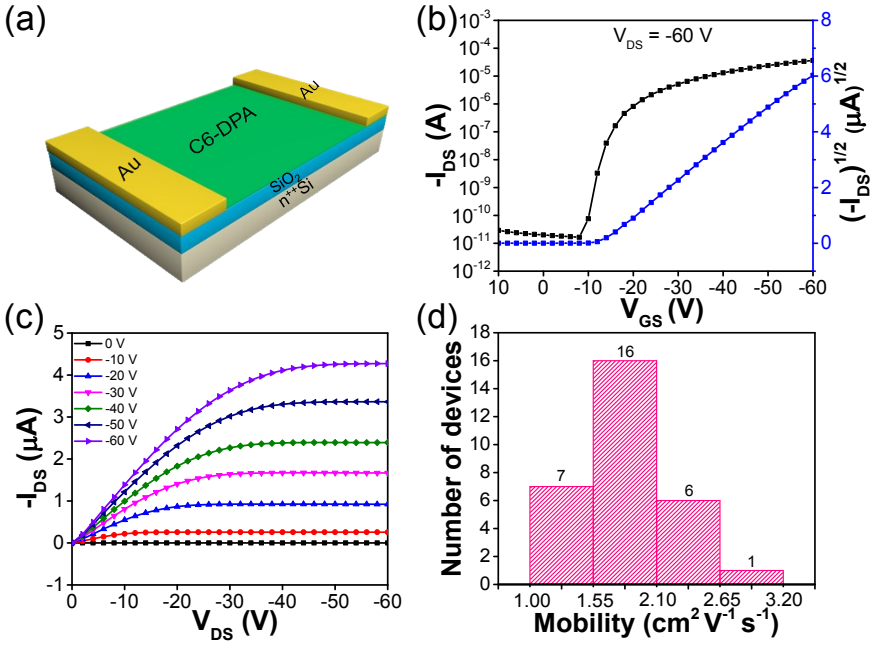

Fig. S12 (a) Schematic of an OFET of 2DMC of C6-DPA. (b) Typical transfer and (c) output curves of 2DMC of C6-DPA. The channel length was 97 μm and the channel width was 105 μm. (d) Histogram of the mobility of 30 C6-DPA OFETs. The average hole mobility was 1.85 cm^2 V^{-1} s^{-1} among 30 devices, and the highest value was 3.16 cm^2 V^{-1} s^{-1}.

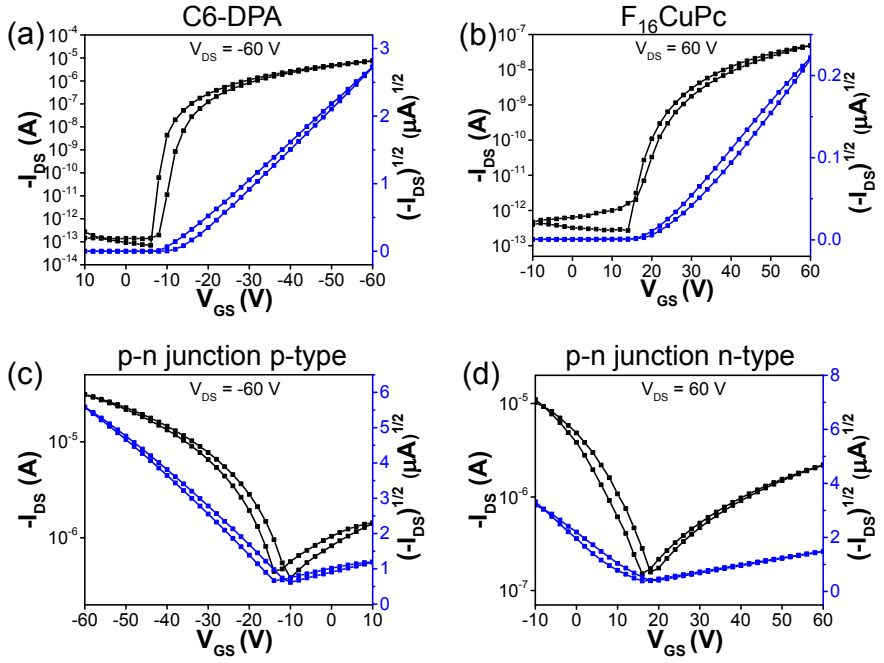

Fig. S13 Hysteresis curves of C6-DPA, $F_{16}CuPc$ and their heterojunction.

The hysteresis curves of C6-DPA, $F_{16}CuPc$ and their heterojunction were shown in Fig. S13. The hysteresis of the p-channel was unchanged after the formation of heterojunction (Fig. S13a, c), which indicated that the quality of the C6-DPA/SiO_2 interface was unchanged. The hysteresis of the n-channel was reduced prominently after the formation of heterojunction (Fig. S13b, d), indicating that the quality of the $F_{16}CuPc$/C6-DPA interface was much better than that of $F_{16}CuPc/SiO_2$ interface.

One main reason for hysteresis of OFETs was charge trapping at the interface of organic semiconductor/dielectric interface.[24-25] The n-channel of heterojunction was in contact with the 2DMCs. Due to the high-quality of 2DMCs, $F_{16}CuPc$/2DMCs interface had fewer electron traps than $F_{16}CuPc/SiO_2$ interface. The other reason was that water and oxygen in the air can induce electron trap centers.[26-27] When $F_{16}CuPc$ was deposited on 2DMCs of C6-DPA, the grain size was large, which protected the film from the air and thus reduced charge trapping.[28-29] As a result, the n-channel of heterojunction aOFETs showed smaller hysteresis than that of single-component OFETs (Fig. S13).

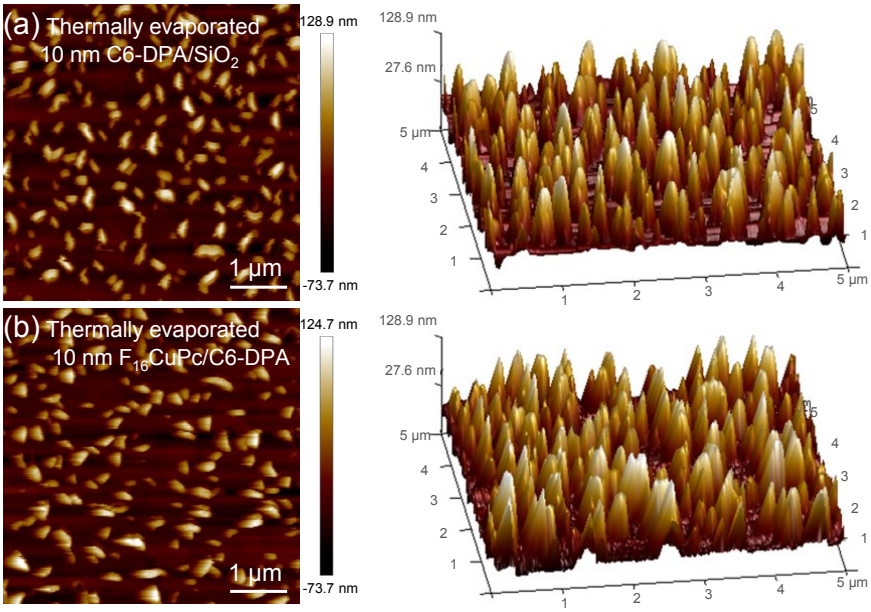

Fig. S14 2D and 3D AFM images of (a) polycrystalline thin film of C6-DPA prepared by thermal evaporation and (b) $F_{16}CuPc$ thermally evaporated on polycrystalline thin film of C6-DPA, respectively.

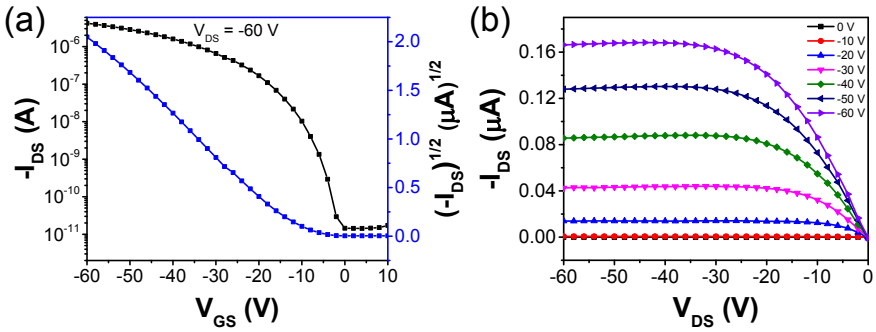

Fig. S15 (a) Transfer and (b) output curves of an OFET based on thermally evaporated C6-DPA on SiO_2. The hole mobility was 0.33 $cm^2 V^{-1} s^{-1}$, which was ~ 10 times smaller than that of 2DMC of C6-DPA (Fig. S12). The channel length was 155 μm and the channel width was 167 μm.

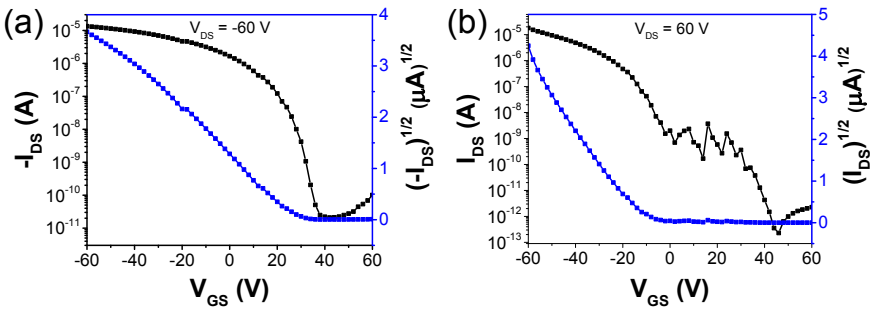

Fig. S16 Typical transfer characteristics of thermally evaporated $F_{16}CuPc$/C6-DPA aOFET under (a) negative and (b) positive drain bias, respectively. The channel length was 155 μm and the channel width was 168 μm.

The transfer characteristics of the two-step vacuum-deposition processed bilayer aOFET exhibited p-channel operation mode only with hole mobility of 0.34 cm^2 V^{-1} s^{-1}, and the n-channel mode was not observed. The poor performance was attributed to the poor morphology of the films and the rough interface between the C6-DPA and $F_{16}CuPc$ (Fig. S14).

Reference

1. Z. Bao, A. J. Lovinger and J. Brown, *J. Am. Chem. Soc.*, 1998, **120**, 207.
2. S. Nénon, D. Kanehira, N. Yoshimoto, F. Fages and C. Videlot-Ackermann, *Thin Solid Films*, 2010, **518**, 5593.
3. C.-L. Tsai, L.-S. Tsai and J.-C. Hwang, *Org. Electron.*, 2012, **13**, 3315.
4. Y. Zhou, S.-T. Han, Y. Yan, L.-B. Huang, L. Zhou, J. Huang and V. A. L. Roy, *Sci. Rep.*, 2013, **3**, 3093.
5. X. Shao, S. Wang, X. Li, Z. Su, Y. Chen and Y. Xiao, *Dyes Pigm.*, 2016, **132**, 378.
6. X. Zhang, Z. Wang, X. Zhou, Z. Wang, L. Huang and L. Chi, *Adv. Electron. Mater.*, 2017, **3**, 1700128.
7. J. Wang, H. Wang, X. Yan, H. Huang and D. Yan, *Chem. Phys. Lett.*, 2005, **407**, 87.
8. R. Ye, M. Baba, Y. Oishi, K. Mori and K. Suzuki, *Appl. Phys. Lett.*, 2005, **86**, 253505.
9. J. Wang, H. Wang, X. Yan, H. Huang, D. Jin, J. Shi, Y. Tang and D. Yan, *Adv. Funct. Mater.*, 2006, **16**, 824.
10. H. Wang, J. Wang, X. Yan, J. Shi, H. Tian, Y. Geng and D. Yan, *Appl. Phys. Lett.*, 2006, **88**, 133508.
11. H. Wang, J. Wang, H. Huang, X. Yan and D. Yan, *Org. Electron.*, 2006, **7**, 369.
12. H. Wang, F. Zhu, J. Yang, Y. Geng and D. Yan, *Adv. Mater.*, 2007, **19**, 2168.
13. J. Shi, H. Wang, D. Song, H. Tian, Y. Geng and D. Yan, *Adv. Funct. Mater.*, 2007, **17**, 397.
14. R. Ye, M. Baba, K. Suzuki and K. Mori, *Appl. Surf. Sci.*, 2008, **254**, 7885.
15. J. Shi, H. Wang, D. Song, H. Tian, Y. Geng and D. Yan, *Thin Solid Films*, 2008, **516**, 3270.

16. W. Gu, X. Li, H. Zhang, B. Wei, J. Zhang and J. Wang, *Thin Solid Films*, 2010, **519**, 439.
17. Y. Zhang, H. Dong, Q. Tang, S. Ferdous, F. Liu, S. C. B. Mannsfeld, W. Hu and A. L. Briseno, *J. Am. Chem. Soc.*, 2010, **132**, 11580.
18. S. Nénon, D. Kanehira, N. Yoshimoto, F. Fages and C. Videlot-Ackermann, *Synth. Met.*, 2011, **161**, 1915.
19. M. Yi, N. Zhang, L. Xie and W. Huang, *J. Semicond.*, 2015, **36**, 104001.
20. S. Huang, B. Peng and P. K. L. Chan, *Adv. Electron. Mater.*, 2017, **3**, 1700268.
21. K. Eguchi, M. M. Matsushita and K. Awaga, *J. Phys. Chem. C*, 2018, **122**, 26054.
22. X. Zhu, Y. Zhang, X. Ren, J. Yao, S. Guo, L. Zhang, D. Wang, G. Wang, X. Zhang, R. Li and W. Hu, *Small*, 2019, **15**, 1902187.
23. Y. Gao, H. Ding, H. Wang and D. Yan, *Appl. Phys. Lett.*, 2007, **91**, 142112.
24. W. Huang, W. Shi, S. Han and J. Yua, *AIP Adv.*, 2013, **3**, 052122.
25. B. M. Egginger, M. Irimia-Vladu, R. Schwödiauer, A. Tanda, I. Frischauf, S. Bauer and N. S. Sariciftci, *Adv. Mater.*, 2008, **20**, 1018.
26. R. D. Pietro and H. Sirringhaus, *Adv. Mater.*, 2012, **24**, 3367.
27. R. D. Pietro, D. Fazzi, T. B. Kehoe and H. Sirringhaus, *J. Am. Chem. Soc.*, 2012, **134**, 14877.
28. C. Qian, J. Sun, L. Zhang, H. Xie, H. Huang, J. Yang and Y. Gao, *Synth. Met.*, 2015, **210**, 336.
29. C. Qian, J. Sun, L. Zhang, H. Huang, J. Yang and Y. Gao, *J. Phys. Chem. C*, 2015, **119**, 14965.